Energy 315 (2025) 134432

Contents lists available at ScienceDirect

Energy

journal homepage: www.elsevier.com/locate/energy

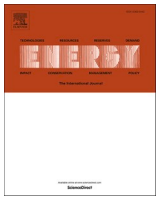

Experimental and numerical study on the mechanical inconsistency of a dual-opposed free-piston Stirling engine generator

Haojie Sun [a,b], Qingyue Jin [a,b], Guoyao Yu [a,c,**], Shunmin Zhu [d,*], Ercang Luo [a,b]

[a] Key Laboratory of Cryogenic Science and Technology, Technical Institute of Physics and Chemistry, Chinese Academy of Sciences, Beijing, 100190, China
[b] University of Chinese Academy of Sciences, Beijing, 100049, China
[c] Institute of Optical Physics and Engineering Technology, Qilu Zhongke, Jinan, 251000, China
[d] Department of Engineering, Durham University, Durham, DH1 3LE, UK

ARTICLE INFO

Keywords:
Energy conversion
Dual-opposed
Free-piston
Stirling engine
Linear generator
Mechanical inconsistency

ABSTRACT

The dual-opposed free-piston Stirling generator (FPSG) presents potential advantages in terms of heightened efficiency, diminished vibrations, and flexible operation. However, the challenge encountered on a dual-opposed configuration posed by components' inconsistency has hindered its progress, and analyses of this inconsistency are infrequently performed in the literature. In response, this study delves into the inconsistency of mechanical parameters, specifically addressing the moving mass of the displacer and the power piston, along with planar spring stiffness, employing both computational modeling and experimental methodologies. A meticulous comparison between experimental outcomes and computational predictions reveals a commendable agreement, with a maximum deviation within 7.3 % for heat-to-electricity efficiency and electrical power. In instances of mechanical inconsistencies, an acoustic power flow within the expansion space transpires, transferring from the generator with a heavier moving mass on the power piston and the displacer, coupled with a stiffer planar spring, to the generator with a lighter moving mass on the power piston and the displacer, along with a softer plate spring. Furthermore, an escalation in the inconsistency of mechanical parameters corresponds to an increased phase difference between the two pistons and the two displacers. It is noteworthy that planar spring stiffness exhibits particular sensitivity to the movements of the moving components. These findings provide valuable perception into the design, manufacture, and control of dual-opposed FPSGs.

Nomenclature

Symbols	
A	cross-sectional area, m^2
Bl	transduction coefficient, V•s/m
C	compliance, m^3/Pa•s
I	current, A
i	imaginary unit
K	stiffness, N/m
L	inertance, kg/m^4
l	length, m
M	moving mass, kg
P	pressure, Pa
Pr	Prandtl number
R	acoustic resistance, Pa•s/m^3
R_m	damping coefficient, N•s/m
R_e	resistance, Ω

(*continued on next column*)

(*continued*)

r_h	hydraulic radius, m
Re	Reynolds number
v	velocity, m/s
U	volume flow rate, m^3/s
V	volume, m^3
X	displacement, m
η	efficiency, %
θ	phase angle, °
μ	dynamic viscosity, kg/(m•s)
ρ	density, kg/m^3
τ	ratio of gas temperatures at the regenerator ends
φ	porosity
ω	angular frequency, 1/s
Subscripts	
b	bounce space
c	compression space

(*continued on next page*)

* Corresponding author.
** Corresponding author.
E-mail addresses: gyyu@mail.ipc.ac.cn (G. Yu), shunmin.zhu@durham.ac.uk (S. Zhu).

https://doi.org/10.1016/j.energy.2025.134432
Received 14 September 2024; Received in revised form 28 November 2024; Accepted 6 January 2025
Available online 7 January 2025

(*continued*)

disp	displacer
e	expansion space
HE	heat-to-electricity
i	internal
load	electrical load
reg	regenerator
rod	displacer rod
serial	series connection
out	outlet
parallel	parallel connection
pist	piston
0	mean
1	first order oscillating value

1. Introduction

Considering the expanding scope of space exploration, it has become imperative to develop space power systems that possess a longer lifespan, higher reliability, and greater power density, capable of meeting the demands of exploration missions [1,2]. Among different space power generation technologies, Stirling power generation technology is a promising candidate for a power level between 0.1 kW–100 kW [3,4].

Stirling power generation technology operates by converting primary energy into mechanical energy through the reciprocating movement of compressible gas under specific pressure within a closed system [5,6]. Subsequently, this mechanical energy is transformed into electrical energy via a linear alternator (LA) and then outputs to loads. The free-piston Stirling generator (FPSG) operates as a resonance system, effectively synchronizing mechanical, electrical, and acoustic resonance to ensure efficient performance [7]. Unlike conventional kinematic Stirling engine-based generators, it dispenses with the crank linkage mechanism, with the moving components supported by planar springs or gas springs [8,9]. This design yields advantages such as a simpler structure, higher operational frequency, and extended lifespan, rendering it better suited for the requirements of space exploration [10,11].

As space exploration extends to more distant realms and human spaceflight progresses, the space power system's capacity and vibration characteristics are subject to heightened demands [12]. The conventional single-piston free-piston Stirling generator (FPSG) is not qualified to meet these demands because of the vibration issues. As a response, the dual-opposed FPSG has emerged due to its capability for higher power output and reduced vibration [13]. In this configuration, two displacers and two pistons are arranged in a straight line, facing each other [14]. Their movements possess the same amplitude but occur in opposite phases, effectively mitigating vibration transmitted to the casing by the moving components. Additionally, the use of a shared expansion space for the two FPSG units enhances the system's volume power density.

Consequently, significant efforts have been dedicated to the development of high-performance dual-opposed FPSGs in recent decades. NASA's Space Power Demonstration Engine (SPDE) consists of two opposed-piston FPSG modules interconnected through a common expansion space, aimed at generating a total electric power output of 25 kW. Operating at a frequency of 100 Hz, the SPDE achieves a power piston displacement of 20 mm and a thermal-to-electric efficiency of 22 % [15]. The displacer stroke is controlled by parasitic damping, which is adjusted by a valve in an external line interconnecting the displacer gas spring chamber and the bounce space. However, this method of adjusting the displacer stroke is unsuitable for dual-opposed FPSGs with planar springs, and the relationship between displacer stroke adjustment and the inconsistency of dual-opposed FPSGs has not been reported. Both Orbital Sciences Corporation (OSC) [16] and Lockheed Martin (LM) [17,18] adopt a dual-opposed configuration to minimize the vibration of FPSG systems. OSC's integrated system achieves a specific power of 8 W/kg with a thermal-to-electric efficiency exceeding 20 %, while LM's system delivers a specific power of 4.2 W/kg and an output electric power of 112 W. NASA Glenn Research Center tested two EG-1000 FPSGs in a dual-opposed configuration using electric heaters for heat input. At a design temperature zone of 823 K/313 K, the two generators produced 2240 W of electricity with an efficiency of 28.6 % [19]. Subsequent enhancements to the heater head and the switch to a sodium-potassium (NaK) heating loop increased the output electric power to 2372 W and the thermal-to-electric efficiency to 32 % [20,21]. Since 2010, Sunpower Corporation has developed a 12-kW dual-opposed FPSG derived from the EG-1000 [22]. Two single-piston FPSG units share a common heating unit, with temperatures set at 850 K at the heater head and 375 K at the heat sink. Their respective output electric powers and thermal-to-electric efficiencies are 6109 W at 26.5 % and 6048 W at 24.4 % [23]. However, further improvements in the consistency of the two FPSG units are needed.

Lin et al. [24] developed a power system including four single-piston FPSGs, where every two FPSGs are in a dual-opposed configuration. The system integrates with potassium heat pipes, with test results demonstrating an output electric power exceeding 300 W and an overall thermal-to-electric efficiency of 7.36 %. Qi et al. [25] developed a 1 kW dual-opposed FPSG, achieving a maximum system efficiency of 25.64 % when the hot-end and cold-end temperatures are 1050 K and 450 K, respectively. However, in simulations, the two FPSGs in the dual-opposed configuration are identical, which is challenging to achieve in experiments. Sun et al. [26] designed a 3 kW dual-opposed FPSG in which the two FPSG units share a common heater and expansion space. Experimental results demonstrated stable operation and attainment of rated power in both series and parallel modes, achieving a thermal-electric efficiency of approximately 25.2 %. Notably, this configuration significantly reduced system vibration, although some phase inconsistencies in the moving parts were observed.

Nevertheless, it is challenging to maintain synchronic operation (of the two single-piston FPSG units) and proper gas exchange in an FPSG with a dual-opposed configuration, and a failure in this would lead to an inconsistent operation and output performance between the two FPSG units. Keeping an appropriate phase difference among the four moving components (two power pistons plus two displacers) is pivotal for the balanced functioning of a dual-opposed FPSG. Any deviation from the required phase relationship could result in diminished engine efficiency and heightened vibration. Alterations in the mass, stiffness, and damping of power pistons and displacers can give rise to uneven forces and vibrations. Additionally, the two displacers must steadily transport the working gas between the hot and cold cylinders during different stages of the cycle. In dual-opposed configurations, ensuring synchronized displacer movement becomes more complex, and any imbalance could disrupt heat transfer and airflow, culminating in the diminished overall performance of the FPSG.

Unfortunately, the issue of mechanical inconsistency in dual-opposed FPSG systems is barely studied. From a traditional perspective, accounting for the interactions between acoustic waves, oscillatory fluid flow, and heat transfer in the analysis of free-piston Stirling engines is challenging. Furthermore, comprehensive experimental and numerical investigations on the influence of mechanical inconsistencies on system performance from a thermoacoustic perspective are lacking. To fill this gap, in this study, taking a 3-kW class dual-opposed FPSG as a case, we use impedance diagrams to qualitatively analyze this inconsistency for the first time. Furthermore, we have comprehensively examined the inconsistency of mechanical parameters, including the moving mass of the displacer and power piston, as well as the stiffness of the planar spring, through a combination of calculations and experiments. Finally, key conclusions are drawn based on the results.

2. System configuration

Fig. 1 illustrates a schematic representation of the 3-kW dual-opposed FPSG. As shown, this FPSG is composed of two identical

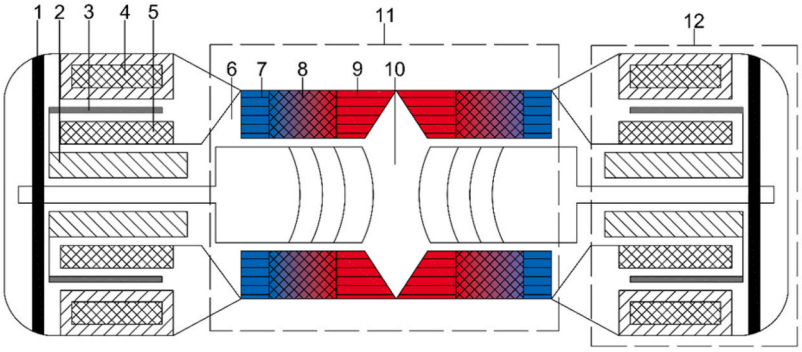

Fig. 1. Schematic diagram of the dual-opposed FPSG, which is composed of two identical single-piston FPSG units.

single-piston FPSG units, each designed at 1.5 kW. The two single-piston units are positioned face to face, sharing a common expansion space. Each unit includes a displacer supported by four planar springs, a power piston, outer stators equipped with capsuled coils, permanent magnets, a compression space, an expansion space, an ambient heat exchanger (AHX), a regenerator and a high-temperature heat exchanger (HHX). The entire FPSG system operates with helium at a pressure of 5 MPa and an operating frequency of approximately 80 Hz. Detailed dimensions for each component of the single-piston FPSG unit are provided in Table 1.

The working principle of the dual-opposed FPSG is as follows: in each single-piston FPSG unit, the working gas is heated by the HHX and cooled via the AHX, which results in a spontaneous thermoacoustic oscillation in the FPSE. The spontaneous thermoacoustic oscillation consecutively converts the external heating power into acoustic power, and when generated acoustic power surpasses the power dissipated by the damping of the parts, the FPSG unit starts. The acoustic power delivered to the regenerator from the compression space is amplified in the regenerator and then transferred to the compression space through the expansion space and the displacer. A part of the acoustic power from the compression space drives the LA to generate electric power, and the remaining acoustic power is delivered to the regenerator again (through the AHX) to be amplified. Two identical single-piston FPSG units can achieve power exchange and heat transfer to each other to keep energy balance in the expansion space. Ideally, the pistons and displacers of the two FPSG units move in the same amplitude and opposed phase to reduce vibration. Fig. 2 gives a photograph of the dual-opposed FPSG prototype.

Table 1
Detailed dimensions for each component of the single-piston FPSG unit.

Component	Variable	Value
	Type	Finned type
HHX	Length/m	0.024
	Heat transfer area/m^2	1.12×10^{-3}
Regenerator	Length/m	0.045
	Sectional area/m^2	5.24×10^{-3}
	Porosity/%	88.5
AHX	Length/m	0.035
	Mean flow area/m^2	3.62×10^{-4}
Displacer	Mass/kg	0.904
	Sectional area facing expansion space/m^2	5.03×10^{-3}
	Sectional area facing compression space/m^2	4.536×10^{-3}
	Spring constant/kN/m	71
Displacer rod	Sectional area/m^2	4.91×10^{-4}
Compression space	Volume/cm^3	93
Expansion space (total)	Volume/cm^3	190
LA	Motor constant/N/A	120
	Internal resistance/Ω	1.17
	Internal inductance/mH	58.48
Power piston	Sectional area/m^2	5.03×10^{-3}
	Moving mass/kg	2.08

3. Numerical and experimental methods

3.1. Numerical methods

To well simulate and capture the mechanical inconsistency between the two single-piston FPSG units, steady-state sinusoidal oscillations of variables such as pressure and velocity are considered, and the governing equations for the displacer based on Newton's second law are expressed as:

$$P_e A_{\mathrm{disp}} - P_c\left(A_{\mathrm{disp}} - A_{\mathrm{rod}}\right) = M_{\mathrm{disp}} i\omega v_{disp} + R_{\mathrm{m-disp}} v_{disp} + \frac{K_{\mathrm{disp}}}{i\omega} v_{disp} \quad (1)$$

$$v_{disp} = \frac{U_{\mathrm{e}}}{A_{\mathrm{disp}}} = \frac{U_c}{A_{\mathrm{disp}} - A_{\mathrm{rod}}} \quad (2)$$

where P_e and U_e represent the oscillating pressure and volume flow rate inside the expansion space, while P_c and U_c refer to the oscillating pressure and volume flow rate inside the compression space. The

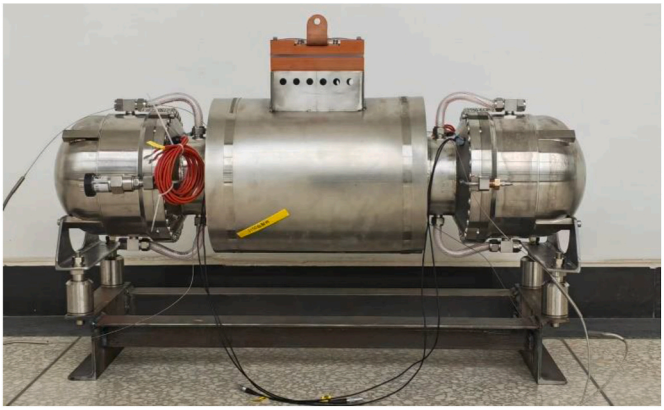

Fig. 2. 3-kWe dual-opposed FPSG prototype.

variables M_{disp}, $R_{m\text{-}disp}$, K_{disp}, and v_{disp} correspond to the mass, damping coefficient, stiffness, and velocity, respectively, of the displacer. Additionally, A_{disp} and A_{rod} are the cross-sectional areas of the displacer and the displacer rod, respectively.

Dividing both sides of Eq. (1) with velocity v_{disp} and combining Eq. (2), we can obtain:

$$\frac{P_e}{U_e}A_{\mathrm{disp}}^2-\frac{P_c}{U_c}\left(A_{\mathrm{disp}}-A_{\mathrm{rod}}\right)^2=M_{\mathrm{disp}}i\omega+R_{\mathrm{m-disp}}+\frac{K_{\mathrm{disp}}}{i\omega} \tag{3}$$

Like electrical impedance, acoustic impedance is defined as oscillating pressure divided by volume flow rate [27]:

$$Z=\frac{P}{U} \tag{4}$$

Consequently, the relation between the impedances at both ends of the displacer and the physical parameters of displacer can be expressed as:

$$Z_eA_{\mathrm{disp}}^2-Z_c\left(A_{\mathrm{disp}}-A_{\mathrm{rod}}\right)^2=M_{\mathrm{disp}}i\omega+R_{\mathrm{m-disp}}+\frac{K_{\mathrm{disp}}}{i\omega} \tag{5}$$

An LA functions as an energy conversion device that transforms acoustic power into electrical power. The electrical connection methods of the two LAs in the external circuit determine the operation state of the dual-opposed FPSG. Similar to the displacer, the power piston's force balance equation can be written as:

$$P_cA_{pist}-P_bA_{pist}=IBl+\frac{K_{pist}v_{pist}}{i\omega}+R_{m-pist}v_{pist}+m_{pist}i\omega v_{pist} \tag{6}$$

where P_b represents the gas pressure amplitude in the bounce space; A_{pist} is the cross-sectional area of the power piston; I, Bl, K_{pist}, v_{pist}, $R_{m\text{-}pist}$, and M_{pist} represent current, transduction coefficient, total stiffness, velocity, damping coefficient, and mass of the piston, respectively.

A capacitor is connected to the other part of the external circuit of the two LAs in series to make the LAs achieving an electric resonant state during operation. Subsequently, under the assumption that the external circuit functions as a purely resistive circuit, the electric balance equation for the two LAs connected in series can be expressed as follows:

$$2Blv=I(R_{e-serial}+2R_i) \tag{7}$$

where $R_{e\text{-}serial}$ and R_i are the external resistance, coil resistance (of each LA), respectively.

Substituting Eq. (6) into Eq. (7), we have:

$$(P_c-P_b)A_{pist}=\frac{Bl^2v_{pist}}{\frac{1}{2}\mathrm{R}_{e-serial}+R_i}+\frac{K_{pist}v_{pist}}{i\omega}+R_{m-pist}v_{pist}+m_{pist}i\omega v_{pist} \tag{8}$$

By dividing both sides of Eq. (8) by the piston velocity *vpist*, Eq. (8) can be reformulated as follows:

$$\left[Z_cA_{pist}A_{pist}-Z_bA_{pist}A_{pist}\right]_{serial}=\left[\frac{Bl^2}{\left(\frac{1}{2}\mathrm{R}_{e-serial}+R_i\right)}+R_{m-pist}\right]+\left[m_{pist}\omega-\frac{K_{pist}}{\omega}\right]i \tag{9}$$

The interpretation of Eq. (9) indicates that the output acoustic impedance of the free-piston Stirling engine (FPSE) is equivalent to that of the LA.

In a similar vein, the impedance balance equation for the two LAs connected in parallel is expressed as follows:

$$\left[Z_cA_{pist}A_{pist}-Z_bA_{pist}A_{pist}\right]_{parallel}=\left[\frac{Bl^2}{\left(2\mathrm{R}_{e-parallel}+R_i\right)}+R_{m-pist}\right]+\left[m_{pist}\omega-\frac{K_{pist}}{\omega}\right]i \tag{10}$$

To enhance the accuracy of calculating the acoustic impedance of the core components within the FPSEs, the commercially available software Sage (developed by Gedeon Associates) was used [28]. SAGE supports the simulation and optimization of customer-designed models, including oscillating flow and heat transfer. It should be noted that Eq. (1) to Eq. (10) were integrated into the SAGE model developed for the prototype. The governing equations of the FPSE are typically represented in a standard format, as shown in Eq. (11) to Eq. (13).

$$\frac{\partial\rho A}{\partial t}+\frac{\partial\rho uA}{\partial x}=0 \tag{11}$$

$$\frac{\partial\rho uA}{\partial t}+\frac{\partial u\rho uA}{\partial x}+\frac{\partial P}{\partial x}A-FA=0 \tag{12}$$

$$\frac{\partial\rho eA}{\partial t}+P\frac{\partial A}{\partial t}+\frac{\partial}{\partial x}(u\rho eA+uPA+q)-Q_w=0 \tag{13}$$

In these equations, the symbols A, u, x, P, q, F, e, and Q_w correspond to cross-sectional area, velocity, axial position, pressure, axial heat flux, pressure drop due to viscosity, internal energy, and heat transfer between the fluid flow and solid surfaces, respectively.

The acoustic impedances of the LAs can be determined using either Eq. (9) or Eq. (10), depending on the electrical connection configuration of the two LAs. In addition, the acoustic impedances of the displacers can be derived from Eq. (5). When the operating parameters are adjusted to ensure that the impedance balance equations are satisfied, the core components of the FPSEs, including the LAs and displacers, achieve optimal matching. Consequently, the parameters of acoustic and flow fields of the whole dual-opposed FPSG can be calculated.

Unlike conventional thermodynamic analysis, the thermoacoustic perspective not only provides a comprehensive view of the dynamic variables throughout the entire engine but also fully accounts for the interplay between oscillatory fluid flow and heat transfer in the form of acoustic resonance and phasing. Key concepts such as acoustic impedance and acoustic power are introduced to offer a clear physical understanding of energy flow matching and energy conversion within the engine.

3.2. Experimental apparatus description

Fig. 3 shows the layout of the dual-opposed FPSG experimental setup which includes a heating sub-system, a load sub-system, a cooling subsystem and a measurement sub-system.

For the measurement subsystem, to measure the output electric power of each single-piston FPSG unit, a voltage transducer and a current probe are deployed in the load circuit of each LA. A power meter is also used to monitor the output electric power of each LA. The wall temperature of the HHX is measured using four K-type thermocouples, and each thermocouple has an accuracy class 1. Average pressure within the system is recorded using two identical pressure transmitters, which are installed in the compression space of each single-piston FPSG unit. Meanwhile, two high-precision dynamic pressure sensors (model: 113B26, from PCB Piezotronics) are installed in each compression space to gauge the dynamic pressure inside the compression space.

For the cooling subsystem, the heat rejected by the two AHXs are absorbed by the cooling water, and the heated cooling water is cooled down by a water chilling unit. Two PT100 thermometers are deployed at the cooling water circulation inlet and outlet of the two AHXs, respectively, to monitor the AHX inlet and outlet temperatures of the cooling water, and a turbine flowmeter is installed in the cooling water circulation circuit, to measure the cooling water's volume flow rate. Therefore, the heat rejected to the cooling water can be measured accordingly. Furthermore, in each single-piston FPSG unit, both the displacer's and the power piston's displacement amplitude and phase angle are individually recorded using an accelerometer (model: M353B18, from PCB Piezotronics).

Regarding the method of phase difference calculation, FFT (Fast

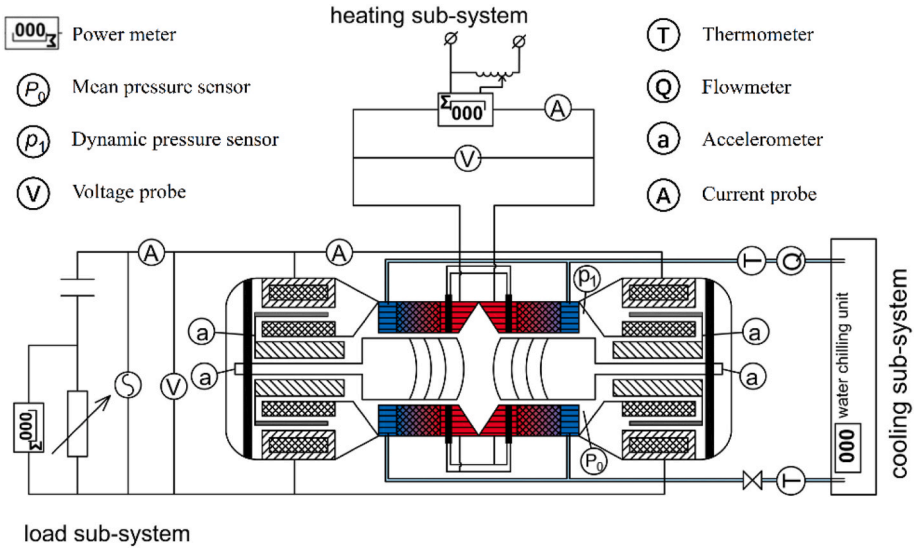

Fig. 3. Layout of the dual-opposed FPSG experimental system.

Fourier Transform) analysis is applied to the synchronous sampling data. As the motions are highly sinusoidal, so the acceleration follows a harmonic approximation, expressed as:

$$a = a_1 e^{i(\omega t+\theta)} \tag{14}$$

As known that displacement is the quadratic integral of acceleration, expressed as:

$$x = -a_1 \omega^2 e^{i(\omega t+\beta)} \tag{15}$$

Clearly, the displacement phase leads the acceleration phase by an angle of "π" (i.e., 180°). Therefore, the phase difference between the displacers can be readily obtained. Fig. 4 displays a typical snapshot of the measured raw acceleration and displacement waves of the moving components (i.e., displacers and pistons).

Enthalpy flow is obtained by extracting the mass flow rate, internal energy, and pressure at the nodes and applying the following equation.

$$E_h = U(e+P) \tag{16}$$

where e is the total energy per specific volume. In the experiment, directly or indirectly measuring the distribution of enthalpy flow based on its physical definition is challenging due to thermal relaxation. However, as indicated in Eq. (17), this enthalpy calculation can be validated by comparing it with the acoustic power in the expansion chamber, given the absence of entropy flow in that region.

$$E_h = Wa + T_0\dot{S} = \frac{1}{2}p_1 U_1 \cos\theta + T_0\dot{m}\dot{s} \tag{17}$$

where E_h, Wa, S are enthalpy flow, acoustic power and entropy flow, respectively.

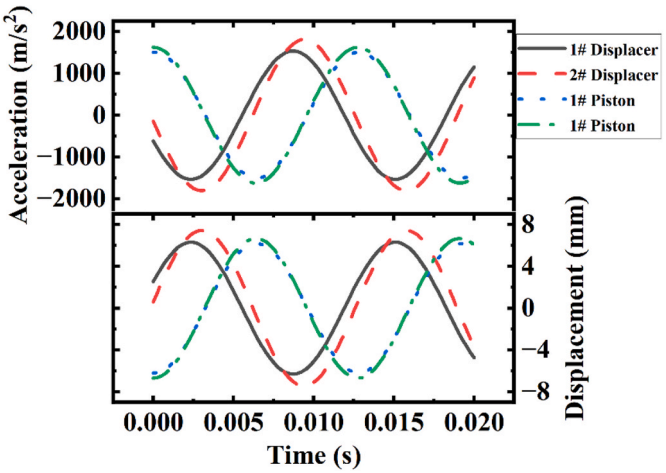

Fig. 4. Measured raw acceleration and displacement waves of the moving components.

3.3. Impedance match in the system

The thermoacoustic theory is a commonly used tool to analysis thermoacoustic engines/refrigerators [29], and Stirling engines/refrigerators [30,31]. From the perspective of thermoacoustics, the key components of these systems can be represented as resistance, capacitance, inductance, or source elements, either individually or a combination of these elements [32,33]. Subsequently, these elements are linked together based on their physical locations, creating an acoustic network diagram. The impedance diagram of the dual-opposed FPSG is shown in Fig. 5. Table 2 lists the expression of the impedance analogy for each element.

The impedance diagram illustrates the fundamental characteristics of the dual-opposed FPSG system, and it serves as a useful tool to explore the influence of structural parameters on the system's performance. Within this diagram, both the compression space and the expansion space can be described as a compliance, with the compliance value being directly proportional to the chamber volume and inversely proportional to mean pressure. Since the two single-piston FPSG units of the dual-opposed FPSG share a common expansion space, the common expansion space can be described as a shared compliance. Utilizing the porous model, the regenerator comprises a viscous resistance, a compliance, and a volume-flow rate source. Notably, both a nonlinear term and a linear term are encompassed within the viscous resistance. Both the AHX and the HHX are modeled as a viscous resistance and a compliance, respectively. The displacer's characteristics are depicted through a series connection of a transformer, a compliance, a resistance, and an inductance. Similarly, the LA can be described as a series connection of an inductance, a resistance, and a compliance. The resistance element encompasses both mechanical resistance and electrical resistance.

4. Results and discussion

The collaborative operation of the four moving components in the FPSG is influenced by a myriad of factors, encompassing mechanical

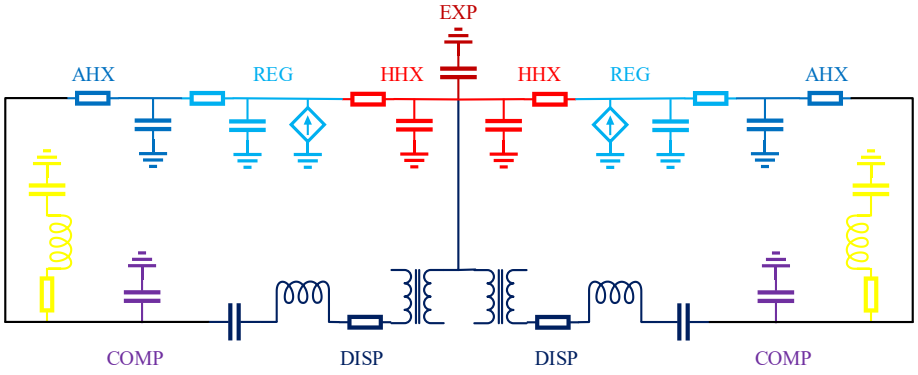

Fig. 5. Impedance diagram for a dual-opposed FPSG.

Table 2
Summary of the acoustic-electric analogy sub-models of each element of the FPSG.

Component	Acoustic-to-electric analogy element
Chamber	$C = \frac{V}{\gamma P_0}$
Regenerator	$R_{\mathrm{REG}} = \frac{(\tau+1)F(\tau,Pr)}{2}\frac{6\mu L}{Ar_h^2} + \frac{4}{3\pi}\frac{(-2.82+10.7\varphi-8.6\varphi^2)\rho_0}{r_h A^2}\frac{(\tau+1)l}{2}\lvert U_1\rvert$ $C_{\mathrm{REG}} = \frac{\tau\ln\tau}{\tau-1}\frac{\varphi AL}{\gamma P_m}$ $\Delta U_{REG} = (\tau-1)U_1$
Heat exchanger	$R = \frac{6\mu_m l}{Ar_h^2}$ $C = \frac{\varphi Al}{p_m}$
Displacer	$C_{\mathrm{d}} = \frac{(A_{\mathrm{disp}}-A_{\mathrm{rod}})^2}{k_{disp}}$ $R_d = \frac{R_{\mathrm{m-disp}}}{(A_{\mathrm{disp}}-A_{\mathrm{rod}})^2}$ $L_{\mathrm{d}} = \frac{M_{\mathrm{disp}}}{(A_{\mathrm{disp}}-A_{\mathrm{rod}})^2}$ $\phi = \frac{A_{\mathrm{rod}}}{A_{\mathrm{disp}}-A_{\mathrm{rod}}}$
Power piston	$R_p = \frac{Bl^2}{(R_{\mathrm{e-load}}+R_{\mathrm{e-i}}+R_{\mathrm{m-pist}})A_{\mathrm{pist}}^2}$ $C_p = \frac{A_{pist}^2}{k_{pist}}$ $L_p = \frac{M_{\mathrm{pist}}}{A_{\mathrm{pist}}^2}$

inconsistency, acoustic component disparity, and variances in heat transfer types. For the sake of experimental convenience and evaluative rigor, this study directs its focus towards examining mechanical inconsistencies, specifically investigating the moving mass of the piston, the moving mass of displacer, and the stiffness of the planer spring. Additionally, controlling the equivalent damping of moving parts in experiments presents challenges; therefore, the impact of damping inconsistencies on system performance is highlighted through computational simulations. This scrutiny aims to analyze their respective impacts on the flow field, acoustic field, and dynamic field.

4.1. Effect of moving mass of displacer

The moving mass of the displacer assembly comprises several components, including the mass of the dome and the rod, as well as a fraction of planar spring mass, reflecting their respective contributions to resonance. Achieving identical moving mass of the two displacers is challenging due to limitations in machining accuracy and measurement precision, making complete consistency of the two FPSG units difficult to attain. Consequently, it is important to evaluate the influence of the discrepancy in moving mass of the two displacers on the consistency of the two FPSG units. In both simulations and experiments, the moving mass of the 1# displacer is fixed at 903 g, while the moving mass of the 2# displacer is intentionally altered to assess the influence of two displacers' moving mass discrepancy on system performance.

Fig. 6 depicts the enthalpy flow distribution and flow chart inside the dual-opposed FPSG with 1014 g moving mass of the 2# displacer. The two LAs are arranged in a series configuration. Notably, the enthalpy flow inside the 1# generator experiences an increase within the expansion space, while the enthalpy flow of the 2# generator suffers from a decrease in the expansion space. Inside the common expansion space, a portion of acoustic power from the 2# generator is transmitted to the 1# generator. This phenomenon is primarily attributed to the greater moving mass of the 2# displacer compared to that of the 1# displacer. As shown in Eq. (5), the impedance amplitude on the expansion space side of the 1# displacer is higher due to its greater mass. On account of the shared expansion space between the two generators, the pressure fluctuations in the expansion space of the two FPSG units remain consistent. Consequently, the volume flow rate demanded by the 2# displacer exceeds that of the 1# displacer, leading to acoustic power transmission from the 2# expansion space (virtual) to the 1# expansion space (virtual).

Fig. 7 illustrates the two displacers' displacement versus the moving mass of 2# displacer. As depicted in Fig. 7, when the two LAs are connected in series, an increase in the moving mass of the 2# displacer results in a linear growth in the displacement of the 2# displacer, while the displacement of the 1# displacer experiences a marginal increase. This implies the sensitivity of the 1# displacer's displacement to the moving mass inconsistency is minimal. The reasons are shown in Fig. 8. Under the rated operation conditions, the equivalent mechanical compliance of the displacer stands at $K_{disp}/\omega = 537$ Pa s/m^3, while the equivalent mechanical inductance is $M_{disp}\omega = 454$ Pa s/m^3. The resultant mechanical impedance of the displacer under the rated condition is represented as the red vector in Fig. 8, in which the dual-opposed FPSG's displacers function as a capacitive load. When the moving mass of the displacer increases, the impedance of the displacer decreases, shown as the black vector in Fig. 8.

In the series connection configuration, with equal transduction coefficients for both linear alternators, the coil current remains the same, resulting in identical forces on both power pistons. This leads to nearly identical pressure fluctuations in the compression chambers of both pistons. Additionally, the displacement of the displacer increases proportionally with the volume flow rate at the ambient end of the displacer.

In a parallel connection, the volume flow rate of the two power pistons becomes equal. As the moving mass of the displacer increases,

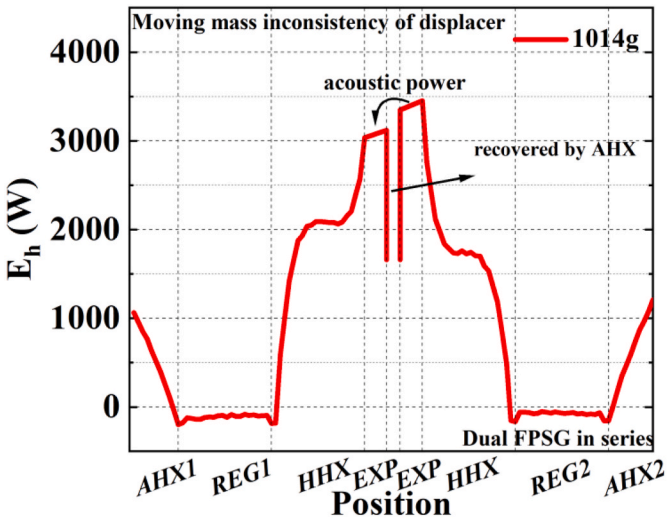

(a) Distribution of enthalpy flow.

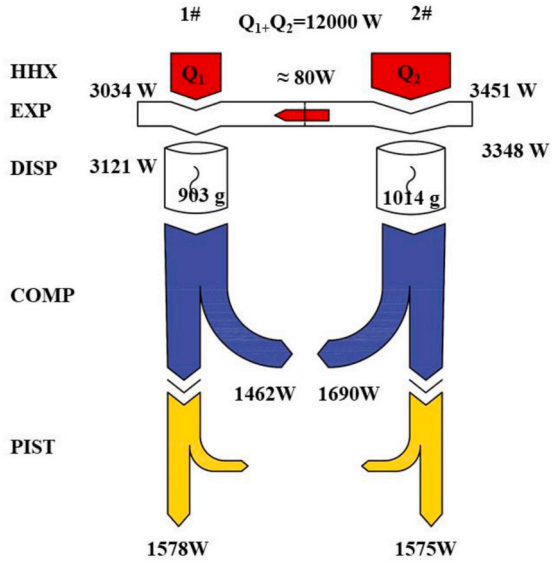

(b) Energy flow chart.

Fig. 6. Distribution of enthalpy flow (a) and flow chart (b) inside the dual-opposed FPSG with 1014 g moving mass of the 2# displacer.

the phase difference between pressure and volume flow in the compression space decreases, which reduces the pressure fluctuations in the compression space. In a constant heat flow scenario, maintaining consistent power generation requires an increase in the displacer's displacement. Since the 2# displacer has a higher volume flow rate compared to the 1# displacer, the 2# expansion space transfers part of the acoustic power to the 1# expansion space, resulting in a slight increase in the displacement of the 1# displacer.

The fundamental distinction between series and parallel connections of linear alternators lies in whether pressure fluctuations or volume flow rate is constrained, which in turn affects the acoustic field within the Free-Piston Stirling Engine (FPSE). While this study maintained constant heat absorption, the significant pressure fluctuations had a substantial impact on the energy flow.

Fig. 9 illustrates how the electrical power output of each single-piston FPSG unit varies with the inconsistency in the moving mass of the displacer. When the two LAs are connected in parallel, within the

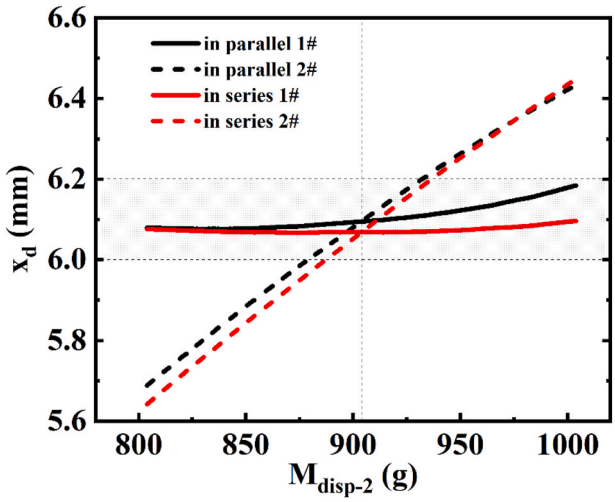

Fig. 7. Displacements of the two displacers versus moving mass of the 2# displacer when the two LAs are connected in series and in parallel, respectively.

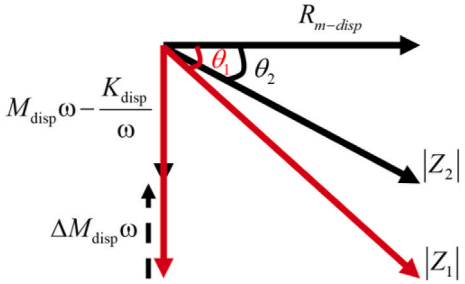

Fig. 8. Equivalent vector diagram of the displacers.

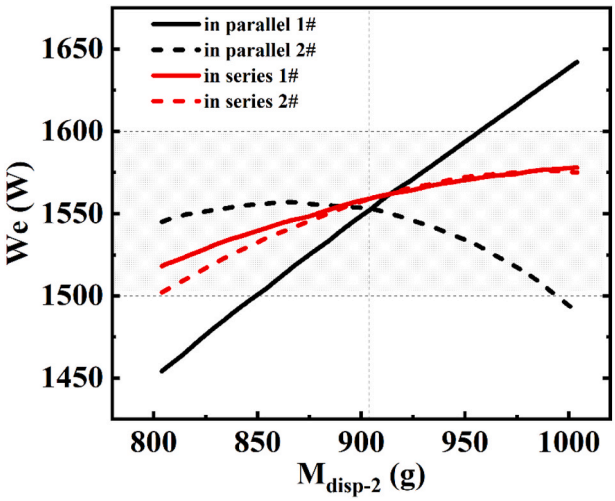

Fig. 9. Electrical power of the two FPSG units versus moving mass of 2# displacer when the two LAs are connected in series and in parallel, respectively.

simulation range, as the moving mass of the 2# displacer increases, the electrical power output on the same side initially rises and then falls, while the electrical power output on the opposite side increases linearly. When the two LAs are arranged in a series configuration, with the increase of the moving mass of the 2# displacer, the electrical power outputs of the two FPSG units both experience a slight increase. It can be concluded that the power generation of the series-connection system displays lower sensitivity to the displacer's moving mass inconsistencies

in comparison with that of the parallel-connection system.

For a parallel-connection system, as the moving mass of the 2# displacer increases, both the pressure fluctuation and the *P-U* phase difference in the compression space of the 2# FPSG unit decrease, while the volume flow rate on the opposite side increases. Based on the acoustic power equation of the piston end (i.e., Eq. (17)), the electrical power output of the 2# FPSG unit first increases and then decreases sharply. Conversely, the acoustic power recovery of the 1# displacer increases, leading to a linear growth in electrical power output. While in a series-connection system, the pressure fluctuations at the power pistons of the two LAs remain consistent. As the moving mass of the 2# displacer increases, the *P-U* phase angle decreases, and the electrical power output gradually increases. Since the heating power at the HHX remains constant, the electrical power output of the two FPSG units tends to stabilize.

Fig. 10 depicts the influence of the moving mass of the 2# displacer on the system's operating frequency and thermal-to-electric efficiency. The system's operating frequency goes down with the increase of the moving mass of the 2# displacer, and for a same moving mass of the 2# displacer, the angular frequency of the parallel-connection system exceeds that of the series-connection system. Within the simulation range, the thermal-to-electric efficiency of the system increases as the moving mass of the 2# displacer grows up. For the angular frequency of the displacer, we have $\omega^2 = 1/2LC$, where acoustic inductance L and acoustic compliance C are extracted from Table 2. Hence, when the displacer's moving mass increases, acoustic inductance L increases, leading to a decrease in operating frequency. With a displacer moving mass of 1 kg, the equivalent mechanical compliance of the displacer remains at $K_{disp}/\omega = 537$ Pa s/m^3, while the equivalent mechanical inductance is $M_{disp}\omega = 496$ Pa s/m^3. The system still operates as capacitive load. The difference between pressure and volume flow rate $\theta_{P\text{-}U}$ decreases as the displacer's moving mass increases, resulting in a monotonic increase in the system's thermal-to-electric efficiency within the investigated range of 2# displacer's moving mass.

Fig. 11 show cases the trend of the phase difference between the two displacers and the phase difference between the two pistons as a function of the moving mass of the 2# displacer. In the scenario that the moving masses of the two displacers are not equal, the phase difference between the pistons and that between the displacers amplifies. If the 1# displacer is heavier than the 2# displacer, the phase angle of 1# displacer leads that of the 2# displacer and the phase angle of 1# piston leads that of the 2# piston, too; conversely, if the 2# displacer is heavier, the movements of the 1# displacer and 1# piston lag that of the 2#

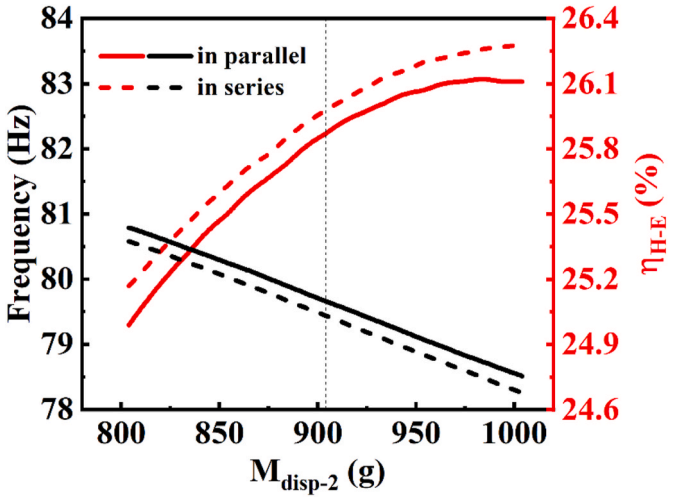

Fig. 10. Operating frequency and heat-to-electricity efficiency versus moving mass of 2# displacer when the two LAs are connected in series and in parallel, respectively.

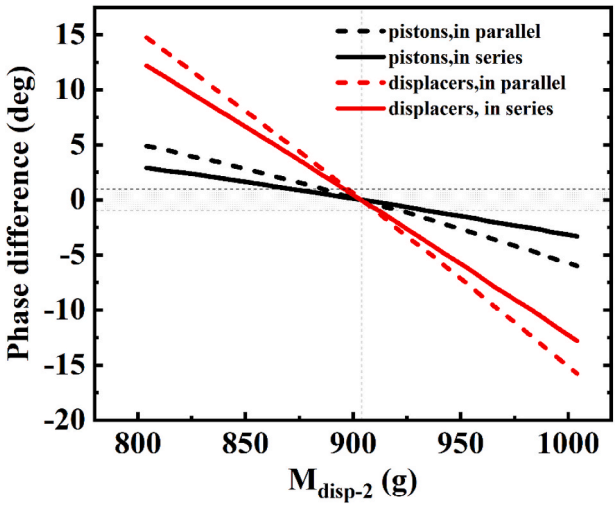

Fig. 11. Phase difference of pistons and displacers versus moving mass of 2# displacer in a series-connection system and in a parallel-connection system, respectively.

displacer and 2# piston. To ensure that the phase difference of the two displacers remains within ±1°, the discrepancy in moving mass between the two displacers in a series-connection system should less than 3.8 %, while in a parallel-connection system, it should less than 2 %. Moreover, to ensure that the phase difference of the power pistons remains within ±1°, the moving mass deviation between the two displacers in the series-connection system should less than 1 %, and in the parallel-connection system, it should less than 0.77 %. This indicates that the in comparison with the series-connection system, the parallel-connection system has a more rigorous requirement on the moving mass discrepancy between the two displacers.

To validate the aforementioned analysis, several experimental case studies were conducted. Table 3 outlines these case studies, demonstrating consistent trends between experimental and calculated results, with deviations in electrical power and thermal-to-electric efficiency keeping within 7.3 %. The two FPSG units with identical displacer weight (0.904 kg) showed a good consistency in performance, featuring a piston displacement deviation of 1.4 % and a displacer displacement deviation of 0.73 %. With the moving mass of 2# displacer increases, electrical power output, thermal-to-electric efficiency, and frequency of the dual-opposed FPSG prototype decrease. In the case that the two displacers' masses are inconsistent, the piston and displacer displacements of the FPSG unit with a heavier displacer are larger than that of the other unit. Meanwhile, the displacer displacement phase of the FPSG unit with a lighter displacer leads that of the FPSG unit with a heavier displacer, which aligns well with the previous analysis (see Table 4).

4.2. *Effect of moving mass of power piston*

The moving mass of the power piston directly impacts the mechanical impedance of the LA, thereby influencing the system performance. Comprising a piston, a permanent magnet, and fixing components, the two power pistons' moving mass consistency relies on machining and assembly accuracy. In practical scenarios, generally, there exists a certain difference in the moving mass of the two power pistons. Therefore, it is important to analyze the influence of the two power pistons' moving mass inconsistency on the overall system. During the analysis process, the moving mass of the 1# power piston was kept at 2083 g. To explore the system's sensitivity to inconsistent piston's moving mass of the two FPSG units, the moving mass of the 2# power piston was adjusted. Under rated operational conditions, the equivalent mechanical compliance of the power piston is $K_{pist}/\omega = 141$ Pa s/m^3, while the equivalent mechanical inductance is $M_{pist}\omega = 1047$ Pa s/m^3, thereby

Table 3
Case studies to estimate the impact of inconsistency of the moving mass of displacer.

Moving mass of 2# displacer (kg)	Method	W_e (W)	η_{HE} (%)	Frequency (Hz)	1# X_{pist} (mm)	2# X_{pist} (mm)	1# X_{disp} (mm)	2# X_{disp} (mm)	$\theta_{d\text{-}d}$ (°)
0.904	simulation	2491	24.91	79.55	5.89	5.89	5.77	5.77	0
0.904	experiment	2490	24.9	79.37	6.48	6.57	6.84	6.79	−2.9
1.004	simulation	2466	24.7	78.31	6.08	6.12	5.35	5.68	−19.3
1.004	experiment	2288	22.9	78.47	6.19	6.67	6.31	7.43	−19.1

Table 4
Impact of inconsistency in the stiffness of the two sets of planar springs on the system performance.

2# planar spring stiffness (kN/m)	Heating power (kW)	W_e (W)	η_{HE} (%)	Frequency (Hz)	1# X_{pist} (mm)	2# X_{pist} (mm)	1# X_{disp} (mm)	2# X_{disp} (mm)	$\theta_{d\text{-}d}$ (°)
272	6	1014	16.9	79.3	5.17	5.33	5.34	5.39	−5
200	6	792	13.2	76.6	5.96	–	5.12	7.34	−68.5

rendering the power piston of this machine an inductive load. The equivalent vector diagram of the power piston is displayed in Fig. 12.

Fig. 13 illustrates the distribution of enthalpy flow inside the dual-opposed FPSG when the 2# power piston's moving mass is 2183 g and the two LAs are connected in series. The enthalpy flow on the side with a heavier moving mass of the power piston notably decreases. An acoustic power flow is observed in the expansion space, transferring from the side with a heavier power piston to the side with a lighter power piston. As shown in Fig. 12, with an increase in the power piston's moving mass, the *P-U* phase difference at the piston end face rises, causing a decrease in the acoustic power at the piston end face during resonance. Consequently, the enthalpy flow inside the generator unit with a moving piston mass of 2183 g is smaller compared to that of the generator unit with a moving piston mass of 2083 g. When maintaining constant regenerator resistance, compliance, inductance, and volumetric flow rate, the greater the piston's moving mass, the smaller the expansion space's volume flow rate. This leads to an increase in the enthalpy flow of 1# generator and a decrease in 2# generator, with a portion of acoustic power flowing from the low volume flow rate side to the higher volume flow rate side.

Fig. 14 presents the displacement and electrical power of the displacer as a function of the 2# power piston's moving mass. As the moving mass of the 2# power piston increases, both the electrical power output of the 2# FPSG unit and the displacer displacement of the 2# generator unit decrease, while the displacer displacement of the 1# generator unit increases. The increase in moving mass results in a lift in the impedance phase (*P-U* phase difference) at the piston's end face (as shown in Fig. 12), thus reducing the conversion of acoustic power into electrical power and generating less electricity. Despite the core unit of the FPSE remaining unchanged, the expansion space's volume flow rate inversely correlates with the power piston's moving mass. Hence, the heavier the power piston, the smaller the displacer displacement. At the side with a lighter power piston, a portion of acoustic power recovery from the 2# generator causes an increase in the displacer displacement of the 1# FPSG unit.

Fig. 15 shows the variation of the phase difference between the two

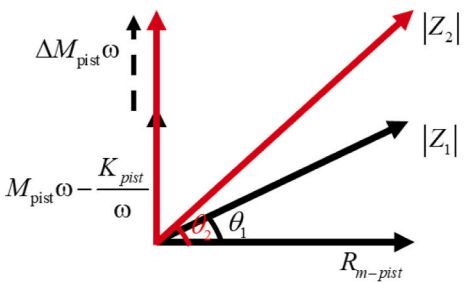

Fig. 12. The equivalent vector diagram of the power piston.

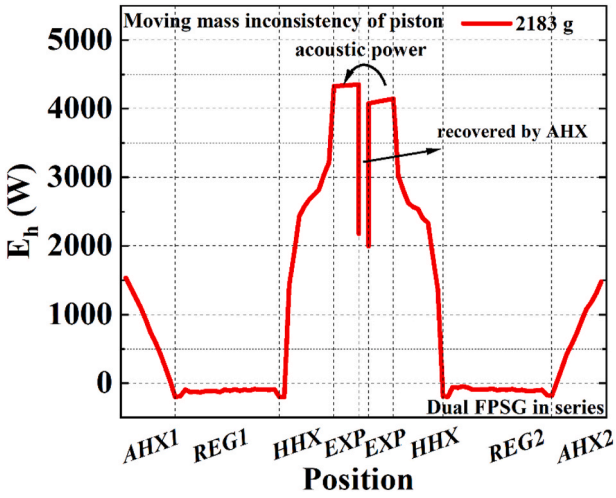

Fig. 13. Distribution of enthalpy flow inside the dual-opposed FPSG when the moving mass of 2# power piston is 2183 g.

displacers and the phase difference between the two pistons under different 2# power piston's moving masses. In the case that the two power pistons' moving masses are not equal, the phase difference between the pistons and that between the displacer escalates. When the 1# power piston is heavier than the 2# power piston, the displacement phase angle of the 1# power piston leads that of the 2# power piston, and vice versa. Similar phenomenon can be also observed in terms of displacer: the displacer's phase of the FPSG unit with heavier power piston lags that of the FPSG unit with a lighter power piston. To ensure that the phase difference of the power pistons remains within ±1°, the moving mass deviation between the two power pistons in the series-connection system should less than 6.3 %, and in the parallel-connection system, it should less than 2.45 %. In addition, to ensure that the phase difference of the two displacers remains within ±1°, the discrepancy in moving mass between the two power pistons in a series-connection system should less than 1.9 %, while in a parallel-connection system, it should less than 1.34 %.

Two different experimental case studies (with moving masses of 2# power piston are 2083 g and 2183 g, respectively) were conducted to verify the simulation model's accuracy. Fig. 16 demonstrates the electrical power output difference and phase difference of the two displacers in relation to heating power at different moving masses of the 2# power piston. As shown in Fig. 16 (a), the electrical power output of the FPSG unit with a heavier power piston diminishes, resulting in $\Delta W_e<0$ when the 2# power piston is 2183 g. The sensitivity of electrical power output in a series-connection system to power piston's moving mass inconsistency is lower than that in a parallel-connection system. With the 2#

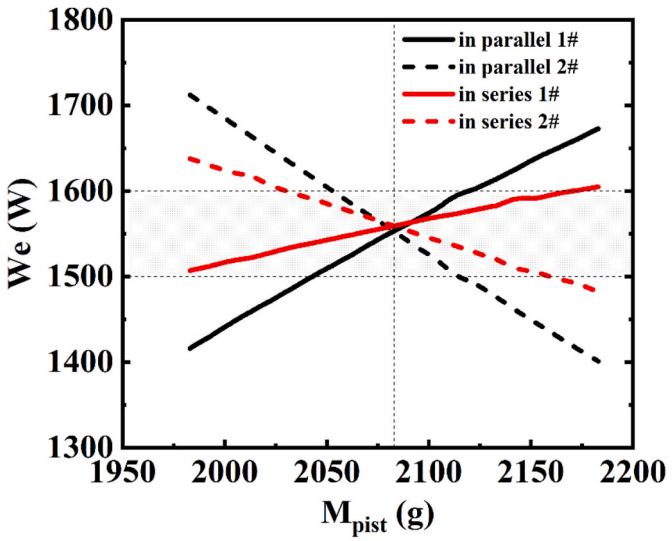

(a) Electrical power output.

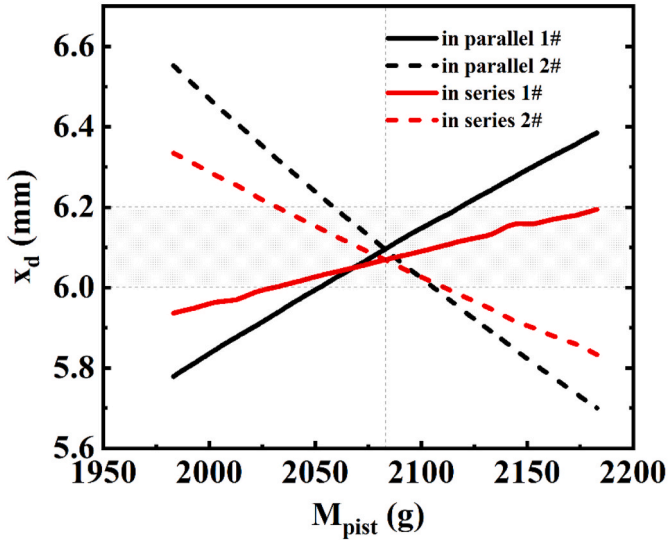

Fig. 14. (a) Electrical power output of the two FPSG units and (b) the displacement of the displacers versus the moving mass of 2# power piston, in a series-connection system and in a parallel-connection system, respectively.

power piston being heavier than the 1# power piston, the 2# displacer's phase angle lags that of the 1# displacer, as shown in Fig. 16 (b). The sensitivity of the two displacers' phase difference in a series-connection system to power piston's moving mass inconsistency is lower than that in a parallel-connection system.

4.3. *Effect of equivalent stiffness of planer spring*

The stiffness of the planar spring plays a pivotal role in determining the mechanical resonance state of the displacer, thereby exerting an impact on system performance. The stiffness of each planar spring is determined by its material, line shape and surface processing technology. However, keeping the total stiffness of the planar springs in the two single-piston FPSG unit (of a typical dual-opposed FPSG) identical is challenging. Consequently, it becomes crucial to assess the impact of inconsistent planar spring stiffness (between the two single-piston FPSG unit) on system performance. In this analysis, the stiffness of the 1# generator's planar spring was fixed at 272 kN/m, while the stiffness of the 2# generator's planar spring was altered to evaluate its effects on the dual-opposed FPSG.

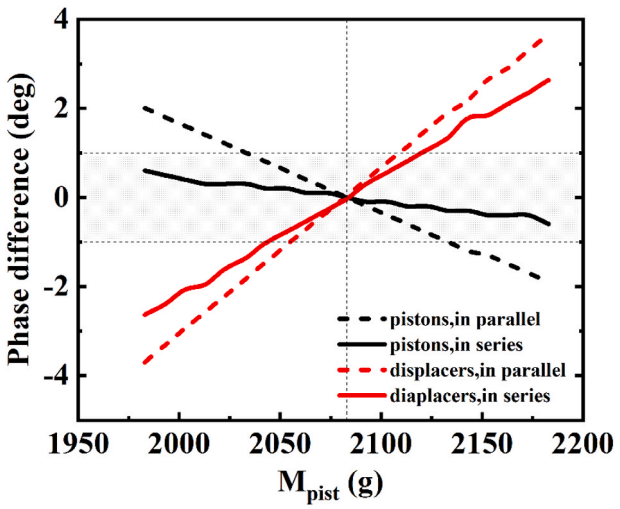

Fig. 15. Phase difference of pistons and displacers versus moving mass of 2# power piston, in a series-connection system and in a parallel-connection system, respectively.

Fig. 17 depicts the distribution of the volume flow rate and the phase difference between oscillating pressure and volume flow rate inside the dual-opposed FPSG with a stiffness of 200 kN/m for the 2# planar spring. It should be noted that the two LAs are connected in series. The overall volume flow rate of 1# generator is higher than that of 2# generator. The phase difference between oscillating pressure and volume flow rate in the core unit of 1# generator ranges from −57° to −35°, whereas in the core unit of 2# generator, it ranges from −32° to 38°.

As illustrated by the black vector in Fig. 18, when the stiffness of the planar spring is 272 kN/m, $M\omega$-$K_{disp}/\omega < 0$, the displacer acts as a capacitive load. Conversely, the red vector in Fig. 18 shows that when the stiffness of the planar spring is 200 kN/m, $M\omega$-$K_{disp}/\omega > 0$, the displacer behaves as an inductive load. The structural parameters and load of the LA determine the oscillating pressure and the volume flow rate at the LA's inlet. Consequently, the impedance phase of the core unit of 2# generator crosses the zero point. When the temperature ratio of the regenerator is constant, the volume flow rate decreases as the acoustic field approaches aa travelling wave phase. Therefore, the volume flow rate of 2# generator, with a planar spring stiffness of 200 kN/m, is smaller than that of the 1# generator.

Fig. 19 depicts the distribution of enthalpy flow inside the dual-opposed FPSG with a stiffness of 200 kN/m for the 2# planar spring. One can see from Fig. 19 that it becomes evident that the enthalpy flow of the 2# generator is smaller than that of the 1# generator. In the expansion space, the enthalpy flow of the 1# generator diminishes, while the enthalpy flow in the expansion space of the 2# generator increases. An acoustic power flow is transferred from the 1# generator to the 2# generator. As shown in Fig. 18, when the planar spring stiffness is 200 kN/m, the impedance amplitude of the displacer is smaller than that of 1# generator, which has a planar spring stiffness of 272 kN/m. Consequently, there is an acoustic power flow in the expansion space transported from 1# generator, with its higher impedance amplitude, to the 2# generator.

Fig. 20 depicts variations in frequency and thermal-to-electric efficiency with different stiffnesses of the 2# planar spring. As the stiffness of the 2# planar spring increases, the system's operating frequency also rises, with the operating frequency of the parallel-connection system exceeding that of the series-connection system. Within the range of the investigated stiffness, the system's heat-to-electricity efficiency first increases and then decreases with the increase of the stiffness of the 2# planar spring.

According to the relationship between the angular frequency of the

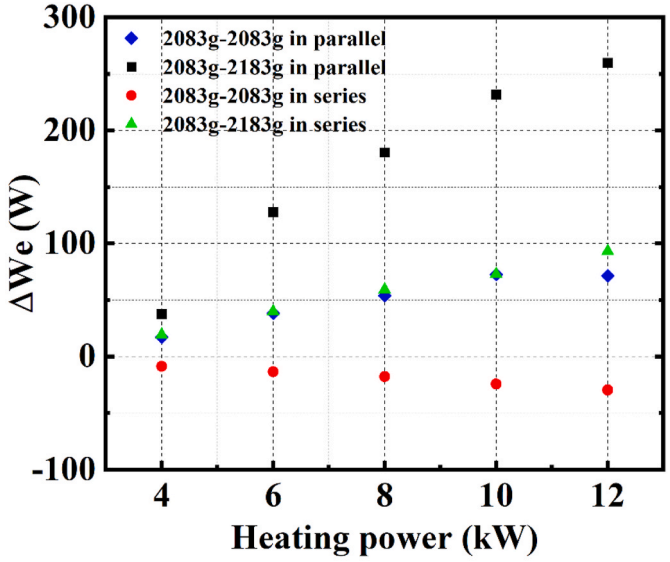

(a) Electric power.

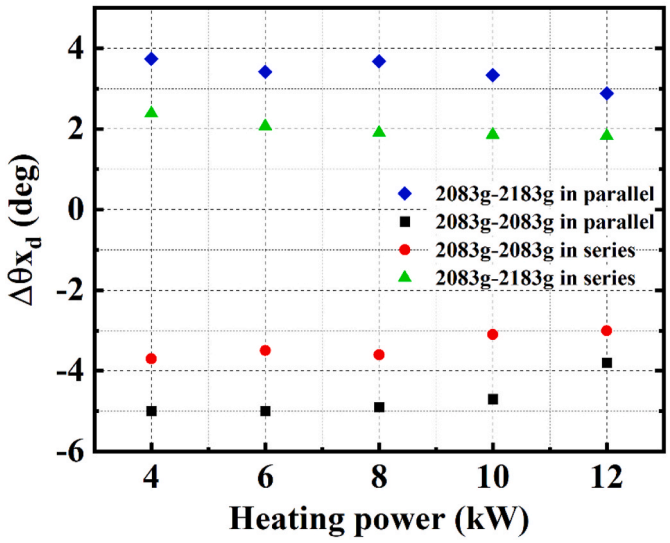

(b) Phase difference.

Fig. 16. Electrical power (a) and phase difference (b) of the two displacers versus heating power in two different experimental case studies (with two different moving masses of power piston).

displacer, acoustic inductance L, and acoustic compliance C, i.e., $\omega^2 = 1/2LC$, an increase in planar spring stiffness results in a decrease in acoustic compliance C and an increase in operating frequency. At a planar spring stiffness of 250 kN/m, where mechanical compliance and mechanical inductance balance out, the displacer operates in a resistive state, yielding the highest efficiency. The efficiency of a series system surpasses that of a parallel system.

Fig. 21 outlines the trend of phase differences between the two displacers and the two pistons as a function of the stiffness of the 2# planar spring. Notably, when the stiffnesses of the two sets of planar springs are unequal, both the phase difference between the two pistons and the phase difference between the two displacers increase. If the stiffness of the 1# planar spring exceeds that of the 2# planar spring, the phase angles of the 1# FPSG unit's power piston and displacer lag behind that of the 2# FPSG unit's power piston and displacer, and vice versa. In a series connection system, the planar spring stiffness deviation is below 3.3 %, while for the parallel system, it's less than 1.5 %. These values

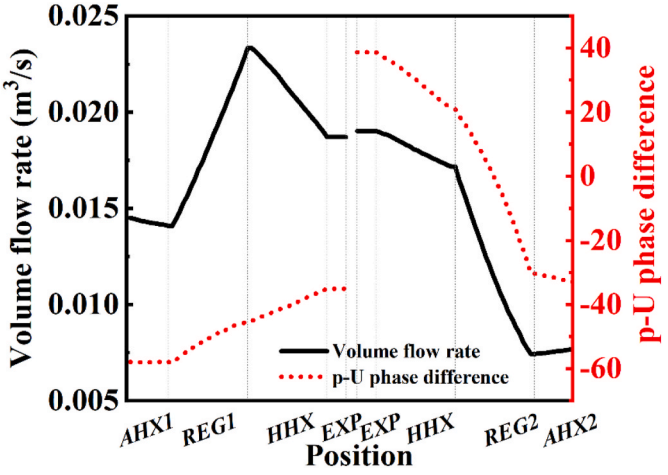

Fig. 17. Distribution of volume flow rate and *p-U* phase difference inside the dual-opposed FPSG when the stiffness of the 2# planar spring is 200 kN/m.

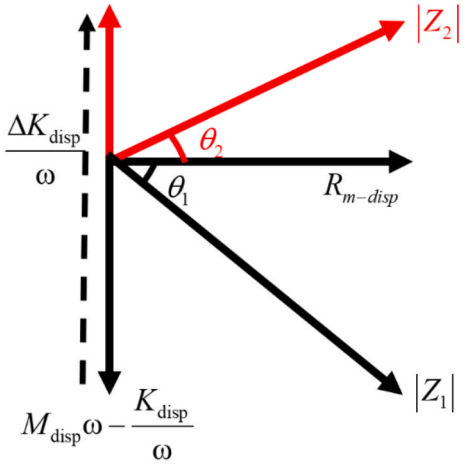

Fig. 18. The equivalent vector diagram of the displacer.

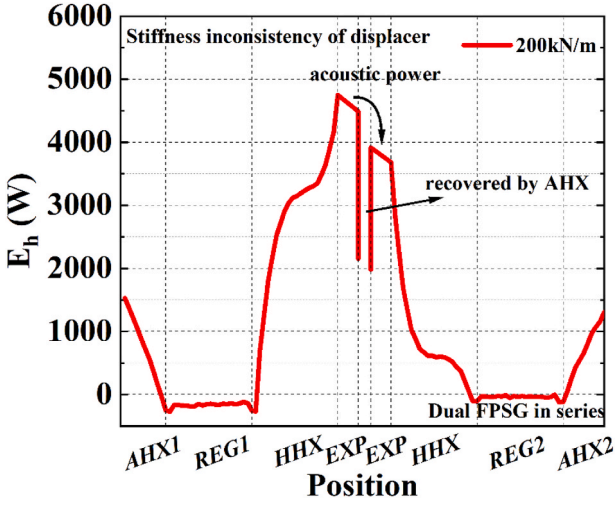

Fig. 19. Distribution of enthalpy flow inside the dual-opposed FPSG when the stiffness of the 2# planar spring is 200 kN/m.

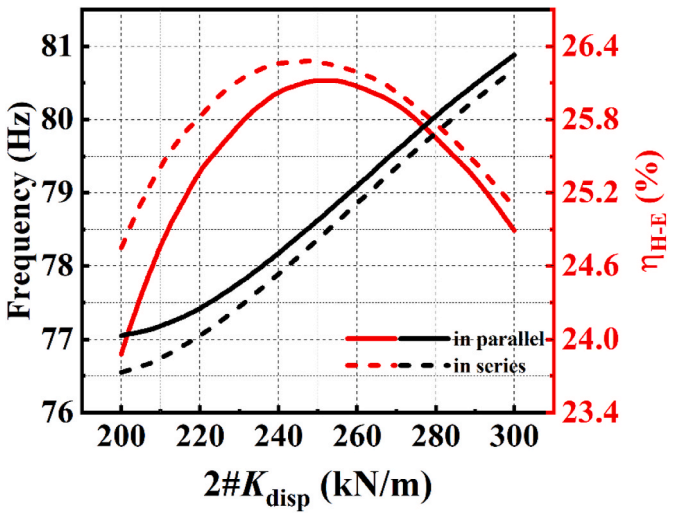

Fig. 20. Frequency and heat-to-electricity efficiency versus 2# planar spring's stiffness, in a series-connection system and in a parallel-connection system, respectively.

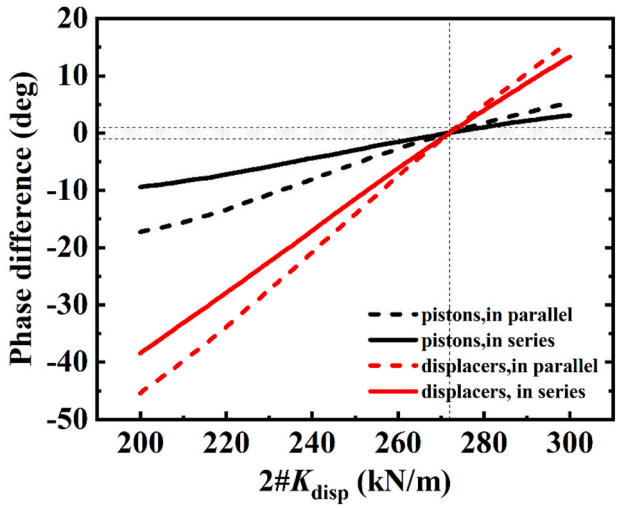

Fig. 21. Phase difference of pistons and displacers versus the stiffness of 2# planar spring, in a series-connection system and in a parallel-connection system, respectively.

ensure that the phase difference between the two displacers remains within ±1°. Furthermore, in a series system, the planar spring stiffness deviation is under 1.1 %, and in the parallel system, it's less than 0.74 %, both ensuring a phase difference between the two power pistons within ±1°.

To explore the effect of inconsistent stiffness of the two generators' planar springs, experiments were conducted by maintaining the 1# planar spring's stiffness unchanged while altering the 2# planar spring's stiffness. In experiments, the 1# planar spring's stiffness was set at 272 kN/m, while the stiffness of the 2# planar spring was set to 200 kN/m. Under this condition, the series-connection system cannot onset when the external resistance was 135 Ω. In contrast, the parallel-connection system starts operation at a temperature of 280 °C in the hot head heat exchanger, with a working frequency of 76.6 Hz. Notably, for the FPSG unit with a larger planar spring stiffness, the displacer's displacement increased significantly, and it led the displacer of the other FPSG unit by 68.48°.

4.4. *Effect of equivalent damping coefficients of moving part*

As indicated in Eq. (9), inconsistencies in the mechanical damping of the displacer and piston affect the acoustic impedance of the dual-opposed FPSG, thereby significantly influencing the motion consistency of the moving components. In practice, however, the inherent randomness of the assembly process makes precise control of damping challenging. This section, therefore, examines the impact of mechanical damping inconsistencies in the piston and displacer on overall system performance.

First, the equivalent damping coefficient of the 1# piston is fixed at 30 N/m, while the damping of the 2# piston is varied to evaluate its effect on system performance. The displacement amplitude difference and phase difference between the 1# and 2# pistons, as well as between the 1# and 2# displacers, are analyzed as functions of the 2# piston's damping. The results are shown in Fig. 22. As the damping difference of the 2# piston increases, the displacement amplitude and phase discrepancies between the moving parts of the two FPSGs also increase,

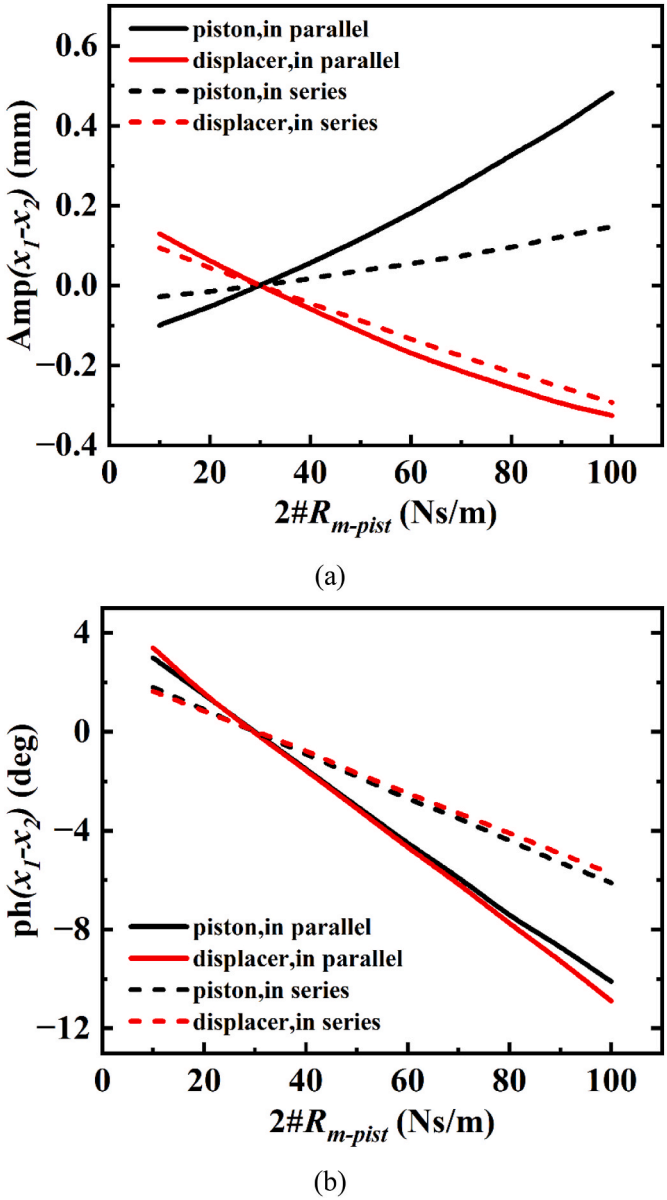

Fig. 22. Amplitude (a) and phase (b) difference of two pistons and two displacers versus the mechanical damping of 2# piston in a series-connection system and in a parallel-connection system, respectively.

leading to more pronounced inconsistencies. When the two alternators are connected in series, system performance is less sensitive to piston damping than when they are connected in parallel. In the series configuration, pressure fluctuations in the 1# and 2# compression chambers are nearly identical. According to Eq. (9), the 2# piston, with higher damping, exhibits smaller displacement, leading to $(x_1-x_2)_{pist}>0$. Additionally, the increased phase lag results in ph $(x_1-x_2)_{pist}<0$. However, the acoustic-to-electric power conversion efficiency of the 2# alternator decreases, requiring greater feedback power to sustain pressure fluctuations in the compression chamber. Consequently, the displacement of the 2# displacer increases, while the 1# displacer leads the 2# displacer in phase.

In the parallel configuration, the trends in displacement inconsistencies between the piston-piston and displacer-displacer pairs are similar to those observed in the series connection. However, in the parallel setup, the external voltage stabilizes the output voltage of both alternators, while differences in the voltage drop across their internal resistances and inductances lead to significant displacement discrepancies between the pistons. The damping and impedance characteristics of the pistons behave similarly to external resistors, and this inconsistency can be mitigated by connecting different electrical resistors in series with each alternator.

Next, the damping coefficient of the 1# displacer is fixed at 15 N/m, with other parameters as specified in Table 1, to evaluate the sensitivity of system performance to displacer damping inconsistencies. The displacement amplitude and phase differences between the 1# and 2# pistons, as well as between the 1# and 2# displacers, are plotted against the damping coefficient of the 2# displacer in Fig. 23. For a fixed heat absorption rate of 12 kW by the shared hot heat exchanger, the 1# displacer and piston exhibit larger displacement amplitudes compared to their 2# counterparts when the mechanical damping of the 2# displacer exceeds that of the 1# displacer. This reduction in displacement for the 2# displacer is primarily attributed to the increased damping, which limits the acoustic power recovery through the 2# displacer. However, acoustic power interactions between the 1# and 2# FPSGs lead to increased displacement amplitudes in the 1# piston and displacer.

The results also reveal that as the damping of the 2# displacer increases, the 2# displacer lags behind the 1# displacer in phase, while the 2# piston leads the 1# piston. Displacer damping inconsistencies have a more pronounced effect on the displacement amplitudes of the moving parts than piston damping inconsistencies, though their influence on displacement phase differences is comparatively weaker.

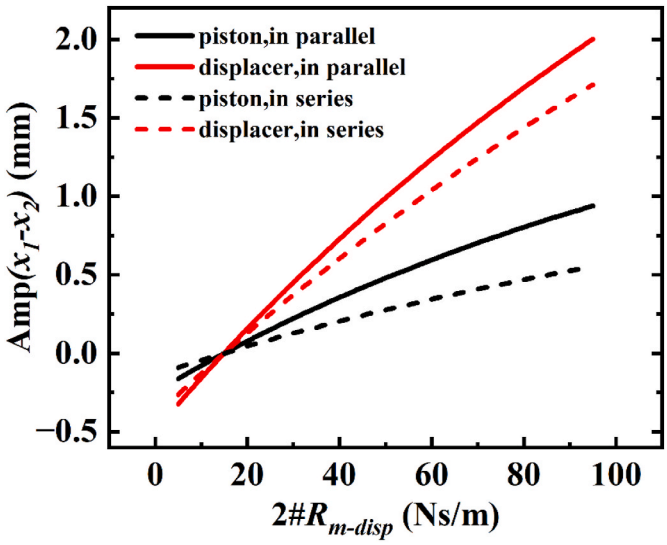

(a) Amplitude difference.

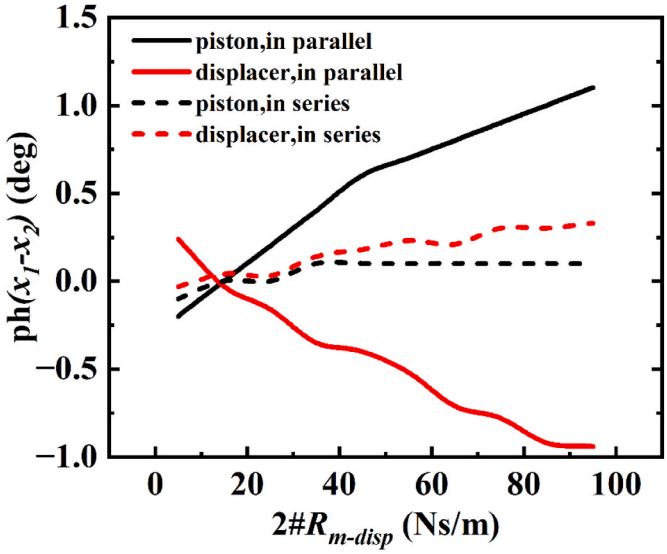

(b) Phase difference.

Fig. 23. Amplitude (a) and phase (b) difference of two pistons and two displacers versus the mechanical damping of 2# displacer in a series-connection system and in a parallel-connection system, respectively.

5. Conclusions

The dual-opposed FPSG configuration comprises two single-piston FPSG units that share a common expansion space. This arrangement combines the advantages of the free-piston design with improved mechanical balance, offering potential enhancements in vibration reduction and operational simplicity. Despite these benefits, the issue of component inconsistency has hindered its development, while the analysis of components' inconsistency is scarce. In this context, we studied the inconsistency of mechanical parameters, such as the moving mass of the displacer and power piston, along with planar spring stiffness, through calculations and experiments.

Upon conducting a thorough comparison between experiments and calculations, we have achieved a remarkable agreement, with a maximum deviation of merely 7.3 % in thermal-to-electric efficiency and electrical power. The impact of mechanical inconsistency on the performance parameters of the two single-piston FPSGs is similarly consistent across both experiments and simulations. In cases of mechanical inconsistencies, an acoustic power flow occurs in the expansion space, transferring from the generator with a heavier dynamic mass in power piston, and stiffer plate spring to the generator with a lighter dynamic mass, power piston, and softer plate spring. Furthermore, heightened mechanical parameter inconsistencies lead to an increased phase difference between the two pistons and two displacers. Notably, planar spring stiffness exhibits the highest sensitivity to the movement of the moving parts.

Through the analysis of mechanical inconsistencies in the dual-opposed FPSG, the impact of parameter variations in the moving components on FPSG performance has been thoroughly characterized. As a result, potential issues stemming from mechanical inconsistencies can be identified through experimental measurement of electrical parameters or displacement of the moving parts. This allows for improved performance consistency by appropriately adjusting these components. Future work will focus on investigating the effect of externally adjustable parameters, such as the load impedance of the two FPSGs, on overall system performance. This will enable the selection of optimal external adjustment strategies to better control inconsistencies and support sustainable, stable operation. Additionally, addressing acoustic

inconsistencies will be crucial, with particular attention to factors such as porosity, Nusselt number, and the flow friction coefficient of the regenerator.

CRediT authorship contribution statement

Haojie Sun: Writing – original draft, Visualization, Software, Methodology, Investigation, Formal analysis. **Qingyue Jin:** Writing – review & editing, Investigation. **Guoyao Yu:** Writing – review & editing, Supervision, Funding acquisition, Conceptualization. **Shunmin Zhu:** Writing – review & editing, Validation, Methodology, Funding acquisition. **Ercang Luo:** Resources, Project administration.

Declaration of competing interest

The authors declare that they have no known competing financial interests or personal relationships that could have appeared to influence the work reported in this paper.

Acknowledgements

This research was financially supported by the National Key Research and Development Program of China (No. 2021YFC28026003) and the National Natural Science Foundation of China (No. 51876214 and No. 52306031).

Data availability

Data will be made available on request.

References

[1] El-Genk MS. Space nuclear reactor power system concepts with static and dynamic energy conversion. Energy Convers Manag 2008;49:402–11. https://doi.org/10.1016/J.ENCONMAN.2007.10.014.
[2] Zhu S, Yu G, Jiang C, Wang T, Zhang L, Wu Z, et al. A novel thermoacoustically-driven liquid metal magnetohydrodynamic generator for future space power applications. Energy Convers Manag 2022;258:115503. https://doi.org/10.1016/J.ENCONMAN.2022.115503.
[3] Mason LS. A comparison of Brayton and Stirling space nuclear power systems for power levels from 1 kilowatt to 10 megawatts. AIP Conf Proc 2001;552:1017–22. https://doi.org/10.1063/1.1358045.
[4] Lange RG, Carroll WP. Review of recent advances of radioisotope power systems. Energy Convers Manag 2008;49:393–401. https://doi.org/10.1016/J.ENCONMAN.2007.10.028.
[5] Zhu S, Yu G, Liang K, Dai W, Luo E. A review of Stirling-engine-based combined heat and power technology. Appl Energy 2021;294:116965. https://doi.org/10.1016/J.APENERGY.2021.116965.
[6] Roy D, Zhu S, Wang R, González-Pino I, Herrando M, Markides CN, et al. Techno-economic and environmental analyses of a solar-assisted Stirling engine cogeneration system for different dwelling types in the United Kingdom. Energy Convers Manag 2024;302:118160. https://doi.org/10.1016/J.ENCONMAN.2024.118160.
[7] Zhu S, Yu G, Ma Y, Cheng Y, Wang Y, Yu S, et al. A free-piston Stirling generator integrated with a parabolic trough collector for thermal-to-electric conversion of solar energy. Appl Energy 2019. https://doi.org/10.1016/j.apenergy.2019.03.169.
[8] Zhu S, Yu G, Jongmin O, Xu T, Wu Z, Dai W, et al. Modeling and experimental investigation of a free-piston Stirling engine-based micro-combined heat and power system. Appl Energy 2018;226:522–33. https://doi.org/10.1016/J.APENERGY.2018.05.122.
[9] Jiang Z, Yu G, Zhu S, Dai W, Luo E. Advances on a free-piston Stirling engine-based micro-combined heat and power system. Appl Therm Eng 2022;217:119187. https://doi.org/10.1016/J.APPLTHERMALENG.2022.119187.
[10] Chi C, Li R, Mou J, Lin M, Jiao K, Yang M, et al. Theoretical and experimental study of free piston Stirling generator for high cold end temperatures. Energy 2024;289:129841. https://doi.org/10.1016/J.ENERGY.2023.129841.
[11] Chen W-L, Currao GMD, Wu C-Y, Evan B, Mao C-Y, Tsai S-W, et al. A study on an unpressurized medium-temperature-differential stirling engine integrated with a new spiral-patterned flat-flame burner and a new spiral-finned hot-end plate. Int J Energy Res 2023;2023:8827094. https://doi.org/10.1155/2023/8827094.
[12] Liu Y, Shen T, Lv X, Zhang G, Wang C, Gu J, et al. Investigation on a lunar energy storage and conversion system based on the in-situ resources utilization. Energy 2023;268:126681. https://doi.org/10.1016/J.ENERGY.2023.126681.
[13] Park J, Ko J, Kim H, Hong Y, Yeom H, Park S, et al. The design and testing of a kW-class free-piston Stirling engine for micro-combined heat and power applications. Appl Therm Eng 2020;164:114504. https://doi.org/10.1016/J.APPLTHERMALENG.2019.114504.
[14] Dadd MW, Bailey PB, Davey G, Davis T, Thomlinson BJ. In: Ross RG, editor. Vibration reduction in balanced linear compressors BT - cryocoolers 11. Boston, MA: Springer US; 2002. p. 175–82. https://doi.org/10.1007/0-306-47112-4_23.
[15] Brown AT. Space power demonstrator engine phase I final report. New york. 1987.
[16] Schock A, Or CT, Kumar V. Radioisotope power system based on derivative of existing Stirling engine. New York, NY (United States): United States: American Society of Mechanical Engineers; 1995.
[17] Cockfield RD. Radioisotope power system options for future planetary missions. AIP Conf Proc 2001;552:740–6. https://doi.org/10.1063/1.1358001.
[18] Lee SM, Jefferey GS. A historical review of brayton and stirling power conversion technologies for space applications. Space Nuclear Conference 2007:No.E-16140.
[19] Kim S, Huth J, Wood J. Performance characterization of sunpower free-piston stirling engines. 3rd int. Energy convers. Eng. Conf. American Institute of Aeronautics and Astronautics; 2005. https://doi.org/10.2514/6.2005-5540.
[20] Briggs M, Geng S, Robbie M. Status of kilowatt-class stirling power conversion using a pumped NaK loop for thermal input. 7th int. Energy convers. Eng. Conf. American Institute of Aeronautics and Astronautics; 2009. https://doi.org/10.2514/6.2009-4597.
[21] Briggs M, Geng S, Pearson J, Godfroy T. Summary of test results from a 1 kWe-class free-piston stirling power convertor integrated with a pumped NaK loop. 46th AIAA/ASME/SAE/ASEE jt. Propuls. Conf. Exhib. American Institute of Aeronautics and Astronautics; 2010. https://doi.org/10.2514/6.2010-7173.
[22] Gary W J, Buffalino A, Holliday E, Penswick B, Gedeon D. Free-piston stirling power conversion unit for fission surface power. Phase I final report. 2010.
[23] Gary W J, John S. Free-piston stirling power conversion unit for fission power system, phase II final report. 2016.
[24] Lin M, Mou J, Chi C, Hong G, Ge P, Hu G. A space power system of free piston Stirling generator based on potassium heat pipe. Front Energy 2020;14:1–10. https://doi.org/10.1007/s11708-019-0655-6.
[25] Qi Y, Sun D, Zhang J. Numerical study on a nuclear-powered Stirling system for space power generation. Appl Therm Eng 2023;233:121140. https://doi.org/10.1016/J.APPLTHERMALENG.2023.121140.
[26] Sun H, Yu G, Zhao D, Zhu S, Dai W, Luo E. Operating characteristics study of a dual-opposed free-piston Stirling generator. Appl Therm Eng 2024;249:123387. https://doi.org/10.1016/J.APPLTHERMALENG.2024.123387.
[27] Gregory W Swift. Thermoacoustics A unifying perspective for some engines and refrigerators. Cham: Springer; 2017. https://doi.org/10.1007/978-3-319-66933-5. 2017.
[28] Sage: Software for Engineering Modeling and Optimization n.d. https://www.sageofathens.com/.
[29] Xiao L, Xu J, Luo K, Chen G, Luo E. Numerical study of a heat-driven thermoacoustic refrigerator based on a time-domain lumped acoustic–electrical analogy model. Energy Convers Manag 2022;268:115982. https://doi.org/10.1016/J.ENCONMAN.2022.115982.
[30] Xiao L, Wu Z, Zhu Q, Jia Z, Zhao D, Hu J, et al. Dynamic response of a dual-opposed free-piston Stirling generator. Energy 2023;284:129253. https://doi.org/10.1016/J.ENERGY.2023.129253.
[31] Zhu S, Yu G, Li X, Ying M, Yan C, Dai W, et al. Acoustic field characteristics of a free-piston Stirling cryocooler with large cooling capacity at liquid nitrogen temperature. Appl Therm Eng 2019;147:324–35. https://doi.org/10.1016/J.APPLTHERMALENG.2018.10.096.
[32] Xiao L, Luo K, Luo E, Xu J. A Summary: dynamic and thermodynamic analysis of thermoacoustic and Stirling systems based on time-domain acoustic-electrical analogy. Appl Energy 2023;347:121377. https://doi.org/10.1016/J.APENERGY.2023.121377.
[33] Sun H, Yu G, Dai W, Zhang L, Luo E. Dynamic and thermodynamic characterization of a resonance tube-coupled free-piston Stirling engine-based combined cooling and power system. Appl Energy 2022;322:119437. https://doi.org/10.1016/J.APENERGY.2022.119437.